Electron tunneling through alkanedithiol self-assembled monolayers in large-area molecular junctions

Hylke B. Akkerman[†], Ronald C. G. Naber[†], Bert Jongbloed[†], Paul A. van Hal[‡], Paul W. M. Blom[†], Dago M. de Leeuw[†‡], and Bert de Boer[†§]

[†]Zernike Institute for Advanced Materials, University of Groningen, Nijenborgh 4, NL-9747 AG, Groningen, The Netherlands; and [‡]Philips Research Laboratories, High Tech Campus 4, NL-5656 AE, Eindhoven, The Netherlands

The electrical transport through self-assembled monolayers of alkanedithiols was studied in large-area molecular junctions and described by the Simmons model [Simmons JG (1963) *J Appl Phys* 34:1793–1803 and 2581–2590] for tunneling through a practical barrier, i.e., a rectangular barrier with the image potential included. The strength of the image potential depends on the value of the dielectric constant. A value of 2.1 was determined from impedance measurements. The large and well defined areas of these molecular junctions allow for a simultaneous study of the capacitance and the tunneling current under operational conditions. Electrical transport for octanedithiol through tetradecanedithiol self-assembled monolayers up to 1 V can simultaneously be described by a single effective mass and a barrier height. There is no need for additional fit constants. The barrier heights are in the order of 4–5 eV and vary systematically with the length of the molecules. Irrespective of the length of the molecules, an effective mass of 0.28 was determined, which is in excellent agreement with theoretical predictions.

dielectric constant | molecular electronics | Simmons model

Thiol-terminated molecules have been of much interest in recent years in the field of molecular electronics, experimentally (refs. 1–5, ref. 6 and references therein, and refs. 7–9) and theoretically (10–15). Theoretical descriptions of electrical transport through molecular wires show that contacts, coupling of contacts to molecules, interface geometries, and vibrations are important in single-molecule experiments (16–21). For studies on a large ensemble of molecules some of these effects will average out over all of the molecules. Consequently, differences in electrical transport between measurements on single molecules and self-assembled monolayers (SAMs) were observed experimentally (ref. 5, ref. 22 and references therein, and ref. 23). Alkane(di)thiols are nonconducting molecules with a bandgap of 8–10 eV (ref. 10 and ref. 22 and references therein) and consist of a saturated carbon backbone with one (or two) thiol end groups. Experimentally, the tunneling current through a monolayer of alkane(di)thiols was shown to be temperature-independent and to decrease exponentially with increasing molecular length (4, 5). The transport has been interpreted in terms of the classical tunneling model through a thin insulating film as provided by Simmons (24, 25). In this model the tunneling current depends on the mean value of the barrier height, allowing for a simplification of the problem of an arbitrarily shaped potential barrier to that of a rectangular barrier. This model has been applied to junctions based on SAMs (4, 26), but an extra fit parameter α is needed to obtain a fit to the measured data. However, as already explained by Simmons (24, 25), for a practical tunnel junction the image potential has to be taken into account. This effect has been neglected in the literature so far.

The system studied in this article is a tunnel junction with an alkanedithiol SAM as the insulating film, a bottom gold electrode, and a highly conducting polymer as a top contact. The polymeric top contact allows for the fabrication of devices with a yield of almost unity for areas up to 100 μm in diameter (5). The highly conducting polymer used is PEDOT:PSS, a water-based suspension of poly(3,4-ethylenedioxythiophene) stabilized with poly(4-styrenesulfonic acid). The polymer acts as a cushion for the thermally evaporated metal atoms to land on and prevents the metal atoms from penetration into the molecular layer. Consequently, the formation of electrical shorts is prevented (27).

Simmons Model

The tunneling current density J through a rectangular potential barrier with height φ_0 is given by (4, 24, 26):

$$J = J_0(\varphi_0 e^{-A\alpha\sqrt{\varphi_0}} - (\varphi_0 + eV)e^{-A\alpha\sqrt{\varphi_0 + eV}}), \qquad [1]$$

where

$$J_0 = \frac{e}{2\pi h(\beta \Delta s)^2} \qquad [2]$$

and

$$A = \frac{4\pi\beta\Delta s\sqrt{2m_e}}{h}, \qquad [3]$$

where Δs is the barrier width at the Fermi level of the electrodes, here equal to the total length s of the tunneling path between the electrodes, m_e is the bare electron mass, V is the applied voltage, and h is the Planck constant. β is a correction parameter, which approaches unity for $V < \varphi_0/e$ (24). α is a unitless constant that was added to provide a way for fitting the tunneling current. The physical meaning of α is still under debate. It might be caused by a nonrectangular barrier shape, the effective mass of the electrons tunneling through the molecules (with $\alpha^2 = m_e^*$), or a combination of both (4, 28). In general, $\alpha = 1$ results in the best fit for the low-voltage range, i.e., $V \leq 0.3$ V. However, to model the current up to 1 V bias, the value of α has to be adjusted. Wang *et al.* (4) obtained for dodecanethiol at low voltages $\alpha = 1$, $\varphi_0 = 0.65$ eV and at higher voltages $\alpha = 0.65$, $\varphi_0 = 1.39$ eV. Li *et al.* (26) obtained similar values, $\alpha = 1$, $\varphi_0 = 0.66$ eV and $\alpha = 0.61$,

APPLIED PHYSICAL SCIENCES

$\varphi_0 = 1.83$ eV, respectively. If we apply this model to our large area junctions with a C12 SAM, values of $\alpha = 1$ and $\varphi_0 = 0.72$ eV are found for $V \le 0.3$ V and $\alpha = 0.53$ and $\varphi_0 = 2.42$ eV for higher voltages. Clearly, there are inconsistencies when applying the rectangular barrier model to molecular tunnel junction characteristics. First, there is no reason for two significantly different barrier heights at a bias $V < \varphi_0/e$. Second, the physical nature of α is unknown, and, finally, the values of the obtained barrier heights between 0.65 and 2.42 eV are much lower than the expected barrier height of 4.5–5 eV as stated earlier. In a molecular tunnel junction based on alkane(di)thiols with Au contacts, the nearest molecular energy level is ≈ 4–5 eV from the Fermi level of the Au contact (10, 28).

An important omission of the classical rectangular barrier model is that the image potential is not taken into account. Incorporating the image force will clearly reduce the height and width of the potential barrier. The image potential V_i is, in good approximation, at distance x from the Au electrode given by (24, 25):

$$V_i = -1.15\lambda \frac{s^2}{x(s-x)}, \qquad [4]$$

where

$$\lambda = \frac{e^2 \ln 2}{8\pi\varepsilon_0\varepsilon_r s}. \qquad [5]$$

Here ε_0 is the permittivity of vacuum and ε_r is the relative dielectric constant of the insulating monolayer. In general, the smaller the value of ε_r, the lower the tunnel resistivity. The potential barrier height at position x is then given by:

$$\varphi(x) = \varphi_0 - eV\frac{x}{s} - 1.15\lambda \frac{s^2}{x(s-x)}. \qquad [6]$$

The mean value of the potential barrier height, including image potential, is given by (24):

$$\bar{\varphi} = \varphi_0 - eV\frac{s_2 - s_1}{2s} - \left[1.15\lambda\frac{s}{s_2 - s_1}\right] \times \ln\left[\frac{s_2(s - s_1)}{s_1(s - s_2)}\right], \qquad [7]$$

where s_1 is the distance between the potential barrier at Fermi level of the contacts and the Au electrode at $x = 0$, and s_2 is the distance from the Au electrode to the potential barrier at the PEDOT:PSS electrode. Thus the width of the barrier Δs at the Fermi level of the Au contact is given by $\Delta s = s_2 - s_1$ (see Fig. 5). After the final calculation of the barrier shape, including the image potential and the mean value of the barrier height, the current density for intermediate voltage range $0 < V < \varphi_0/e$ is given by (24):

$$J = J_0(\bar{\varphi}e^{-A\sqrt{\bar{\varphi}}} - (\bar{\varphi} + eV)e^{-A\sqrt{\bar{\varphi}+eV}}), \qquad [8]$$

where A is given by Eq. **3** in which the bare electron mass is replaced by m_e^*, the electron effective mass.

Impedance Measurements

To determine the strength of the image potential, we first have to determine the value of the dielectric constant ε_r. To do accurate impedance measurements on a monolayer, both the tunneling current and capacitance need to be measured for sufficiently large areas. Previously, the capacitance was measured electrically in so-called hanging mercury drop electrode experiments, resulting in a dielectric constant for alkane(di)thiols ranging from 2.0 to 2.7 (9, 29). In large-area molecular junctions (Fig. 1), both the device area and the thickness of the monolayer are well defined. The device areas, defined in vertical
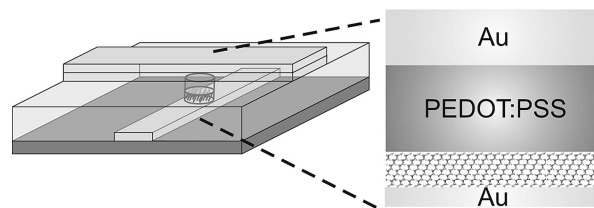

Fig. 1. Schematic representation of a large-area molecular junction. The SAM is formed on the bottom Au electrode in a vertical interconnect in photoresist. On top of the SAM the highly conducting polymer PEDOT:PSS is spin-coated, preventing electrical short formation when the top Au layer is thermally evaporated.

interconnects in photoresist, range from 7.1×10^{-11} to 7.8×10^{-9} m^2 (for diameters of 10–100 μm). Therefore, the capacitance and the tunneling current can be measured *in situ* for different device areas. For the impedance measurements the junctions were processed on 4-inch Pyrex wafers (Silicon Quest International, Santa Clara, CA). The use of nonconducting Pyrex wafers eliminates parasitic capacitances that originate from the highly doped silicon wafers that we used as substrates in our previous work (5). The impedance measurements were done under high vacuum ($< 10^{-6}$ mbar) with a SI 1260 Impedance/Gain-Phase Analyzer (Solartron, Hampshire, UK), at 0-V dc bias and 100-mV ac in a frequency range of 100 Hz to 7 MHz. Fig. 2 shows the typical output characteristics of measurements (data points) on a C14 SAM for different device areas. Fig. 2a shows the absolute magnitude of the impedance $|Z|$ as a function of frequency, and the phase of the signal versus the frequency is plotted in Fig. 2b. The impedance and phase characteristics are subsequently fitted (solid lines) with an equivalent circuit shown in Fig. 2b Inset. Here, the resistance of the monolayer is depicted by the resistor R_{SAM}, in parallel with the total capacitance C_{TOT} and a series resistance R_S. R_S represents the resistance of the contacts and the wiring, which is very small compared with R_{SAM} ($R_S \ll R_{SAM}$). The total capacitance measured C_{TOT} consist of
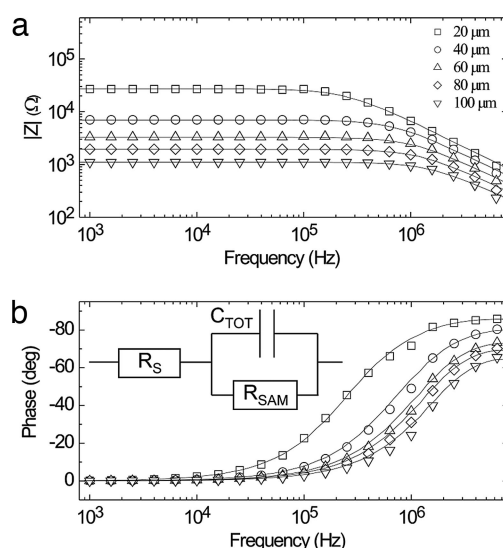

Fig. 2. Output characteristics of impedance measurements at 0-V bias on a C14 SAM for five different devices with diameters of 20–100 μm. (*a*) The measured absolute magnitude of the impedance $|Z|$ versus the frequency of the ac signal. The fit results are plotted as solid lines. (*b*) The phase difference plotted versus frequency. (*Inset*) The equivalent circuit used for modeling the data. The total capacitance measured (depicted by C_{TOT} in the equivalent circuit) consists of two parallel capacitances, i.e., the capacitance of the monolayer C_{SAM} and the capacitance of the photoresist C_{RES}.

Akkerman *et al.*

two parallel capacitances, i.e., the capacitance of the monolayer C_{SAM} and the capacitance of the photoresist C_{RES}. The thickness of the photoresist (570 nm) is much larger than the thickness of the SAM. However, because of the relatively large overlap of the bottom and top electrode of 0.23 mm^2, the capacitance of the photoresist cannot be disregarded. This parasitic capacitance was determined separately by impedance measurements on Au/photoresist/PEDOT:PSS/Au structures without holes in the photoresist layer. With the determined dielectric constant of the photoresist of 5.3, the total capacitance measured can be corrected for this parallel capacitance C_{RES} to obtain the capacitance of the SAM (C_{SAM}). The capacitance of the SAM is calculated by $C_{SAM} = C_{TOT} - C_{RES}$, where the device area should be subtracted from the area of the overlapping bottom and top electrode to calculate C_{RES}. The measured resistive-capacitive ($R \times C$) time constant of this equivalent circuit is therefore not independent of device area, because the area of the parallel capacitance C_{RES} reduces with increasing device area.

The impedance (see Fig. 2a) is constant at low frequency and decreases linearly with increasing frequency. The constant value of the impedance at lower frequencies is determined by the value of R_{SAM}. From the slope of the impedance versus frequency in the higher frequency range, where the phase difference approaches $-90°$, the value of the total capacitance C_{TOT} can be calculated. Because of the series resistance R_S the phase is not saturating at maximum frequency at $-90°$ but at a lower value. With increasing the device area (or decreasing R_{SAM}) the effect of the series resistance R_S will be more profound and the phase will saturate at lower values. The transition frequency (f_T) at which the impedance will change from constant value (dominated by the resistance of the SAM) to a lower and frequency-dependent value (dominated by the total capacitance) is an important parameter for showing the limitations and requirements of capacitance measurements on single molecular layers. When the device area is increased, the device resistance R_{SAM} will decrease and f_T will shift to higher frequencies, as shown in Fig. 2a. The maximum frequency is fixed at 7 MHz and limited by the measurement set-up. Therefore, the frequency range and the accuracy for determining the capacitance will decrease with increasing device area. When the f_T is at 2 MHz, half a decade in frequency range (2–7 MHz) is available to calculate the capacitance with reasonable accuracy. A maximum f_T of $\approx$2 MHz corresponds to a device where the monolayer in the device has a resistance of $\approx$1 kΩ. For an accurate measurement of the capacitance of a C14 SAM, the upper limit of 2 MHz for f_T corresponds to a device with a diameter of $\approx$100 μm. Besides an upper limit in device area, the lower limit in device area results from the overlap of the top and bottom electrode, as discussed above. When the diameter of the device is <10 μm, the parallel capacitance caused by the Au/photoresist/PEDOT:PSS structure is much larger than the capacitance of the monolayer, resulting in a large error in the determined capacitance of the monolayer and, consequently, a less accurate measurement of the dielectric constant. Taking into account the above-mentioned considerations, our research for C12 SAM and C14 SAM junctions is limited to devices with a diameter in the range of 10 to 100 μm.

In Fig. 3 the capacitance of the C14 SAM is plotted versus device area. The data points and the error bars represent the average value and standard deviation of at least eight different devices for each area. From the slope of the linear fit through the data points, the relative dielectric constant can be calculated by using a thickness d of the monolayer, which is given by the length l of the molecules and their tilt angle of 30° via $d = \cos(30) \times l$. Although the surface of our Au bottom electrodes evaporated on SiO$_2$ is not atomically flat, the gold surface has a dominant (111) orientation. Alkane(di)thiols are tilted 30° from the normal to the surface when the monolayer is adsorbed on Au (111) (refs. 6 and 30 and references therein and ref. 31). The length of
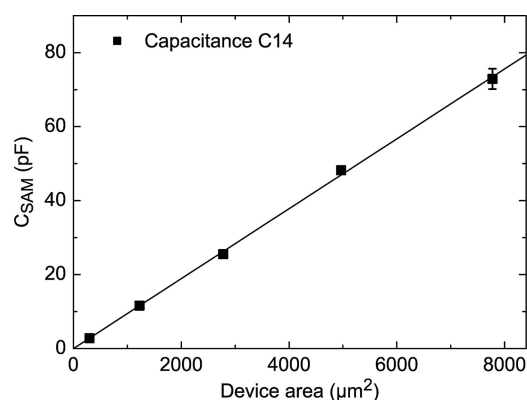
Fig. 3. The measured capacitance for a C14 SAM plotted versus device area. The error bars give the standard deviation upon averaging over at least eight devices. The linear fit to the data results in a dielectric constant of $\varepsilon_r = 2.09 \pm 0.05$.

C14 molecules (including a 2.3-Å Au—S bond) was calculated to be 22.6 Å by using ACD/Labs 8.00 software, resulting in a thickness d of the SAM of 19.6 Å. Using this value of d, a dielectric constant $\varepsilon_r = 2.09 \pm 0.05$ was calculated from the slope of the linear fit. This value is in good agreement with the value determined previously from the hanging mercury drop electrode experiments, where a value ranging from 2.0 to 2.7 was obtained (9, 29). For C12 we obtained a similar value of $\varepsilon_r = 2.01 \pm 0.08$. To verify that the impedance measurements are temperature-independent, the capacitance of the SAM was measured in the range of 200 to 300 K. For this temperature range the dielectric constant was temperature-independent within experimental error.

The resistance will decrease with increasing dc voltage, because the tunneling current increases exponentially with applied field. In the impedance measurements this will lead to a shift of f_T to higher frequencies. Therefore, measurements at higher dc bias are limited to C14 SAMs. The resistance R_{SAM} at different dc bias can be determined from the modeling with the equivalent circuit. Because the obtained resistance R_{SAM} from the impedance measurements at certain applied dc bias equals dV/dI for that specific applied voltage, integration of dI/dV versus V will result in the original current–voltage (I–V) characteristic. This is shown in Fig. 4, where the current of a C14 SAM with diameter 20 μm is calculated from the impedance measurements. Compared with the separately and directly measured dc I–V characteristic for positive applied bias, both methods result in exactly
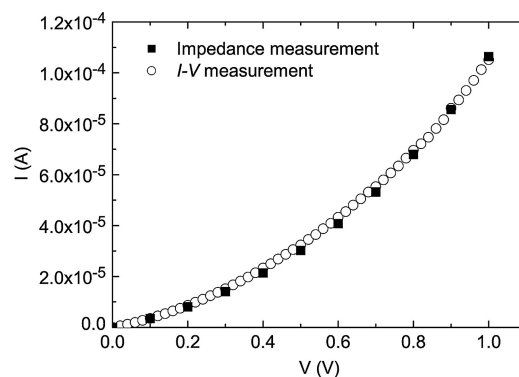
Fig. 4. The directly measured I–V characteristic compared with the current calculated from the impedance measurements at different dc voltages for a device with diameter 20 μm for a C14 SAM. The perfect agreement between both methods demonstrates the consistency of the impedance measurements.
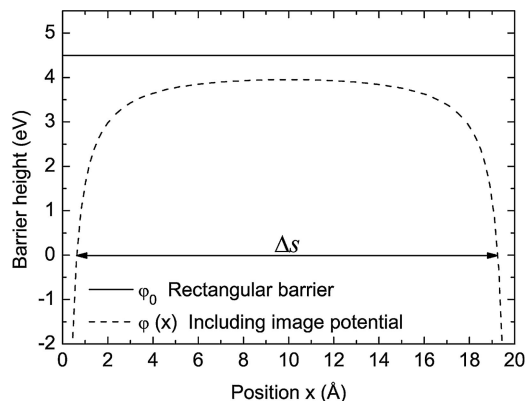
Fig. 5. An illustration of the effect of the image potential on the potential barrier shape. The rectangular barrier (solid line) at 4.5 eV is lowered, rounded at the corners, and the barrier width, Δs, at the Fermi level of the contacts is reduced.

Fig. 6. Current density J plotted versus the applied voltage V for four different molecule lengths, ranging from C8 to C14. The error bars represent the standard deviation upon averaging over at least 17 devices. By incorporation of the image potential to the rectangular barrier model, and using an electron effective mass of 0.28, all of the J–V characteristics are accurately described in the voltage range of −1-V to 1-V bias.

the same I–V characteristic, showing the consistency of the measurements. A change in relative dielectric constant with increasing electric field, i.e., with increasing dc voltage, was not observed within the error of the measurement.

Electrical Transport

Now that we have established the dielectric constant of an alkanedithiol monolayer to be 2.1, the strength of the image potential at position x in the potential barrier can be calculated by using Eq. **4**. To illustrate the significant effect of the image potential on the rectangular potential barrier shape (Fig. 5), we calculate the image potential for a dodecanedithiol molecule (C12; length 19.9 Å) between two contacts. The Fermi level of both contacts is positioned at 0 eV. The nearest molecular energy level, i.e., the height of the rectangular barrier, φ_0, is chosen to be 4.5 eV from the Fermi level of the contacts.

The resulting potential barrier is rounded at the corners, and the total area under the potential barrier is strongly reduced compared with the initial rectangular barrier. In total, these effects will strongly enhance the probability for a charge carrier to tunnel through the barrier. Two fit parameters were used for the final modeling: φ_0, defining the initial rectangular potential barrier height without image force incorporated, and m_e^*, the electron effective mass. φ_0 is the energy difference between the nearest molecular energy level and the Fermi energy level of the Au electrode. Because the work function of PEDOT:PSS (5.2 eV) is 0.2 eV larger than the work function of gold (5.0 eV), the potential barrier at the PEDOT:PSS electrode is also 0.2 eV higher. The electron effective mass originates from the periodicity in the alkane backbone, where one unit cell is composed of two carbon atoms (10). In Fig. 6 the J–V characteristics are plotted for four different molecule lengths ranging from C8 to C14 together with the modeling results using the Simmons model, including image potential with a dielectric constant of 2.1 that was measured before.

Table 1 summarizes the effective mass and the barrier heights used to fit the tunneling current for the four different SAMs. Interestingly, all J–V characteristics measured on different molecule lengths (C8, C10, C12, or C14) are well described by using only one unique electron effective mass of $m_e^* = 0.28\,m_e$. For effective masses <0.25 m_e or >0.30 m_e it is not possible to model the J-V characteristics. Remarkably, this result is exactly equal to the theoretically predicted value of the electron effective mass by Tomfohr and Sankey (10), using a complex band structure for n-alkanes of infinite length. They found, using minimal basis set calculations, an electron effective mass of $m_e^* = 0.29\,m_e$ with a
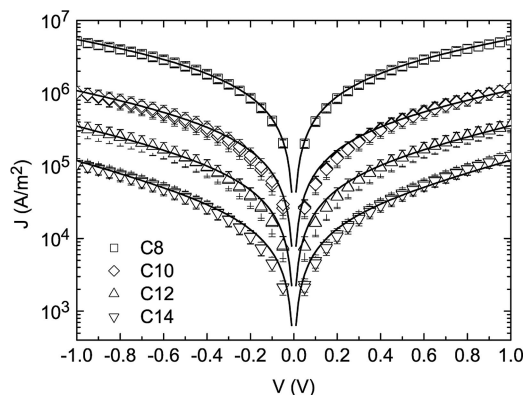
band gap $E_g = 10.25$ eV. The calculated band gap is approximately twice φ_0, because the Fermi level of the contact is situated in the middle of the band gap (10, 28). Extended basis calculation resulted in $m_e^* = 0.28\,m_e$ with a band gap $E_g = 9.75$ eV. The obtained electron effective mass is comparable to the electron effective mass used in ultrathin SiO_2, with a typical value of $m_e^* = 0.30\,m_e$ (32, 33).

Fig. 6 demonstrates that the measured J–V characteristics can be described with the Simmons model when the image potential is included in the model. The fit to the data are accurate within the error of measurement over the full voltage range up to 1-V bias.

Thus, in contrast to the rectangular tunneling model, the voltage dependence of the tunnel current is described with only one barrier height in both the low (<0.3 eV) and intermediate voltage regime (0.3–1 V). Furthermore, there is no need for the additional fit parameter α. However, the obtained barrier heights, φ_0, at the Au/molecule interface decrease with increasing molecule length, ranging from 5.59 eV for C8 to 3.62 eV for C14. Although the obtained barrier heights are in the same range as the expected barrier height of ≈4–5 eV, the systematic decrease of the barrier height with increasing molecule length has no physical origin. Contrary to conjugated molecules, insulating molecules such as alkanedithiols do not exhibit a decrease of the bandgap with an increasing length of the backbone. Even for polyethylene, which can be regarded as a very long alkane, Fujihira and Inokuchi (34) measured with photoemission spectroscopy a large bandgap of 8.0 eV and ionization potential of 8.5 eV.

Table 1. Modeling results using the Simmons model with image potential included

SAM	Length, Å, including 2.3-Å Au–S	φ_0, eV	m_e^*	ε_y
HS-C_8H_{16}-SH	14.8	5.59	0.28	2.1
HS-$C_{10}H_{20}$-SH	17.4	4.82	0.28	2.1
HS-$C_{12}H_{24}$-SH	19.9	4.16	0.28	2.1
HS-$C_{14}H_{28}$-SH	22.6	3.62	0.28	2.1

Results were obtained by fitting the measured J–V characteristics with the Simmons model, including image potential. φ_0 and m_e^* are the used fit parameters. φ_0 decreases with increasing molecule length from 5.59 eV for C8 to 3.62 eV for C14. The best fit to the data was obtained with an electron effective mass of 0.28 for all molecule lengths.
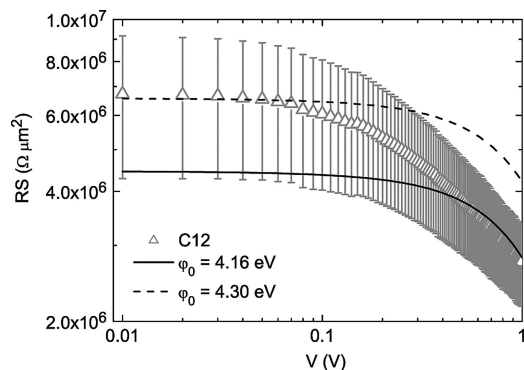
Fig. 7. Resistance R multiplied with the device area S on a log-scale plotted versus applied voltage on a log-scale for a C12 monolayer. This representation reveals the details of the low-voltage regime. Up to $\approx$0.3-V bias, the fit with a barrier height $\varphi_0 = 4.16$ eV (solid line) obtained by fitting the J–V characteristic (Fig. 6) is not in good agreement with the measurement, and only at bias from 0.3 to 1 V the Simmons model fits the measurement. An even larger discrepancy between model and experiment is obtained when the Simmons model is used to fit the low-voltage regime, with a barrier height $\varphi_0 = 4.30$ eV (dashed line).

We have demonstrated that, apart from the apparent decrease of the barrier height with molecule length, the Simmons model with the image potential and effective mass incorporated clearly provides an improved description of the experimental J–V characteristics as compared with the rectangular barrier model. However, we also want to place a critical note regarding the validity of the Simmons model in the low-voltage regime. As a first step we replot the experimental data; the resistance R multiplied with the device area S on a log scale is now plotted versus the applied voltage on a log scale, as depicted in Fig. 7 for a C12 monolayer. This representation, introduced by Simmons in his original papers (24, 25), especially reveals the details of the low-voltage regime. In contrast to Fig. 6 where the fit seems accurate in the whole bias regime, Fig. 7 directly shows that the shape of the fit from Simmons with a barrier height $\varphi_0 = 4.16$ eV (solid line) does not accurately represent the complete shape of the experimentally obtained J–V. Up to $\approx$0.3-V bias, the fit is not in good agreement with the measurement, and only at bias from 0.3 to 1 V the Simmons model fits the measurement. With solely the barrier height and the effective mass as a fit parameter we find that it is not possible to simultaneously describe both the low ($<$0.3 V) and high ($>$0.3 V) bias regime with the Simmons model. A fit with the Simmons model for the low-voltage regime with a barrier height of 4.30 eV is also plotted in Fig. 7 (dashed line). For this barrier height the discrepancy between model and experiment is even larger, and the model does not describe the data over the full voltage range, within the error of measurement. This discrepancy has not been noted so far in literature to our knowledge, because the published data are plotted in current (density)–voltage graphs. Representation of the data in RS versus log V plots would be beneficial for further understanding of the transport mechanisms in tunnel junctions based on SAMs.

To summarize, we have applied the Simmons model, i.e., a rectangular potential barrier combined with the image potential, to the J–V characteristics of alkanedithiols in large-area molecular junctions. The strength of the image potential is determined by the dielectric constant. From impedance measurements we obtained a dielectric constant of 2.09 ± 0.05 for C14 and 2.01 ± 0.08 for C12. The model describes the data up to 1-V bias, without any additional fit parameters besides the barrier height and the electron effective mass. We obtained barrier heights ranging from 5.59 eV for C8 to 3.62 eV for C14. Irrespective of the length of the molecules, the data measured were in agree-

Table 2. X-ray photoelectron spectroscopy results obtained on a monolayer of C12-dithiol from ethanol onto a gold surface at 45°

		C 1s			S 2p	
Peak	Au 4f	C_xH_y	C-O	O 1s	C-S^H	Au-thiol
Energy, eV	84.0	284.8	286.3	533.0	163.5	161.9
HS-C$_{12}$H$_{24}$-SH, int.	35.4	55.6	—	2.5	3.8	2.4

Taking into account the reduced S intensity (int.) for the Au-thiol, the ratio between S-Au and ^{H}S-C becomes 1, implying a complete formation of the standing-up phase.

ment with the modeling when using an unique electron effective mass of 0.28 m_e. Although theory and experiment are apparently in agreement for the full voltage range up to 1-V bias, a more detailed investigation by plotting RS versus V reveals a disagreement between the Simmons model and the experimental data. For voltages $>$0.3 V the Simmons model with the image potential incorporated gives a good description of tunneling currents in molecular junctions, although the obtained decrease in potential barrier height with increasing molecule length remains unclear.

Experimental Procedures

The so-called large-area molecular junctions, schematically depicted in Fig. 1, are processed similarly to a previously described method (5). A 4-inch silicon wafer with 500 nm thermally grown oxide is passivated by using hexamethyl disilazane for a better adhesion of the spin-coated photoresist. An adhesion layer of 1 nm Cr and 60 nm Au are thermally evaporated through a shadow mask. The typical rms roughness of the Au bottom contact is 0.5 nm for 1 μm^2. Subsequently, negative photoresist (ma-N 1410) diluted with Thinner ma-T 1014 (7:1 ratio) is spin-coated on the wafer, resulting in a layer thickness of 570 nm. A prebake step at 95°C at a hotplate eliminates the remaining solvents in the layer. Lithography is done with a MA1006 mask aligner (Karl Süss, Garching, Germany). Vertical interconnects (or vias) are created by photolithography on top of the bottom Au electrodes, with a diameter ranging from 10 to 100 μm. After fabricating the vertical interconnects, the photoresist is annealed for 1 h at 200°C in vacuum to make the photoresist insoluble in ethanol. The complete wafer is then submersed for a minimum of 36 h in the solution of the self-assembling molecules in ethanol. The synthesis of the molecules is done as described (5). The concentration of the molecules in ethanol is 3×10^{-3} M. After the self-assembly of the alkanedithiolate on the Au bottom electrode, the wafer is thoroughly rinsed with ethanol, toluene, and *iso*-propanol to remove the remaining alkanedithiol molecules. Subsequently, the water-based suspension of PEDOT:PSS is spin-coated. For this work, the commercially available Baytron P HC V4 (H.C. Starck, Goslar, Germany) was used with a conduction of $\approx$20 S/cm. To decrease the surface tension of the PEDOT:PSS and improve the wetting on the SAM in the vertical interconnects, a surfactant (FSO Zonyl 100; DuPont, Wilmington, DE) is added. Immediately after spin coating, the PEDOT:PSS layer is dried in a vacuum chamber. Next, a 150-nm Au top electrode is thermally evaporated on top of the PEDOT:PSS layer. The Au top electrode ensures a better contact with the probes when devices are measured in a probe station under vacuum, but also serves as an etching mask in the final processing step. With reactive ion etching redundant PEDOT:PSS is removed to prevent any parasitic currents from top to bottom electrode.

Adsorption of HS-C_xH_{2x}-SH (Cx-dithiol) from ethanol onto a gold surface results in a monolayer with one thiol bonded to gold, the so-called standing-up phase (28, 35–39). X-ray photoelectron spectroscopy (XPS) is a versatile surface technique that discriminates between chemisorbed S-Au (S2p: 161.9 ± 0.1 eV) versus unbound S-C (S2p: 163.5 ± 0.1 eV), and is used to validate the orientation of the monolayers. SAMs of C12-dithiol are prepared on UV oxygen-cleaned gold films. Monolayers are prepared from solution in ethanol at a 3 mM concentration at room temperature. The incubation time for these monolayers is >20 h, after which the samples are rinsed with ethanol and dried with a nitrogen gas flow. For analysis, the samples are transported in air for 10 min, minimizing the amount of oxidation. XPS data in Table 2 show that the amount of ^HS-C is even somewhat higher than the amount of S-Au. Taking into account the somewhat more reduced S intensity for an Au-thiol compared with the intensity for the outer C-S^H, the ratio between S-Au and S-C is 1, implying a complete formation of the standing-up phase. Moreover, the coverage and the layer thickness can be predicted by using a four-layer model for the standing-up phase onto Au (S/C/S/Au) (40). The layer thickness is ≈ 2.0 nm (± 0.2), and the calculated coverage is 4.5×10^{14} molecules per cm^2. The latter is in excellent agreement for a maximum coverage of alkane-(di)thiols on Au being 4.6×10^{14} cm^{-2} (ref. 6 and references therein and ref. 41). A calculated layer thickness of 2 nm is in good agreement for a standing-up phase of C12 dithiol on Au. From ellipsometry measurements a layer thickness of 1.9 nm is calculated.

In addition to C12, we used alkanedithiols ranging from 1,8-octanedithiol (C8) to 1,14-tetradecanedithiol (C14), which corresponds to a tunnel barrier width between 14.8 and 22.6 Å. Because vapor deposited Au has a work function ≈ 5 eV (3) and PEDOT:PSS has a work function of ≈ 5.2 eV, the modeling was done according to the Simmons model for dissimilar electrodes (25). For clarity the theoretical work of Simmons is explained first for similar electrodes. It should be noted that the small difference in work function of ≈ 0.2 eV will not lead to any significant changes.

1. Fenter P, Eisenberger P, Liang KS (1993) *Phys Rev Lett* 70:2447–2450.
2. Cui XD, Primak A, Zarate X, Tomfohr JK, Sankey OF, Moore AL, Moore TA, Gust D, Harris G, Lindsay SM (2001) *Science* 294:571–574.
3. de Boer B, Hadipour A, Mandoc MM, van Woudenbergh T, Blom PWM (2005) *Adv Mater* 17:621–625.
4. Wang W, Lee T, Reed MA (2003) *Phys Rev B* 68:035416.
5. Akkerman HB, Blom PWM, de Leeuw DM, de Boer B (2006) *Nature* 441:69–72.
6. Love JC, Estroff LA, Kriebel JK, Nuzzo RG, Whitesides GM (2005) *Chem Rev* 105:1103–1169.
7. Kushmerick JG, Holt DB, Pollack SK, Ratner MA, Yang JC, Schull TL, Naciri J, Moore MH, Shashidhar R (2002) *J Am Chem Soc* 124:10654–10655.
8. Haynie BC, Walker AV, Tighe TB, Allara DL, Winograd N (2003) *Appl Surf Sci* 203–204:433–436.
9. Rampi MA, Schueller OJA, Whitesides GM (1998) *Appl Phys Lett* 72:1781–1783.
10. Tomfohr JK, Sankey OF (2002) *Phys Rev B* 65:245105.
11. Xue Y, Datta S, Ratner MA (2002) *Chem Phys* 281:151–170.
12. Galperin M, Nitzan A, Ratner MA, Stewart DR (2005) *J Phys Chem B* 109:8519–8522.
13. Sun Q, Selloni A, Scoles G (2005) *ChemPhysChem* 6:1906–1910.
14. Wold DK, Haag R, Rampi MA, Frisbie CD (2002) *J Phys Chem B* 106:2813–2816.
15. Seminario JM, Yan L (2005) *Int J Quantum Chem* 102:711–723.
16. Mujica V, Kemp M, Ratner MA (1994) *J Chem Phys* 101:6849–6855.
17. Galperin M, Ratner MA, Nitzan A (2005) *Nano Lett* 5:125–130.
18. Grigoriev A, Sköldberg J, Wendin G, Crljen Z (2006) *Phys Rev B* 74:045401.
19. Joachim C, Ratner MA (2005) *Proc Natl Acad Sci USA* 102:8801–8808.
20. Damle P, Ghosh AW, Datta S (2002) *Chem Phys* 281:171–187.
21. Basch H, Cohen R, Ratner MA (2005) *Nano Lett* 5:1668–1675.
22. Salomon A, Cahen D, Lindsay SM, Tomfohr JK, Engelkes VB, Frisbie CD (2003) *Adv Mater* 15: 1881–1890.
23. Selzer Y, Cai L, Cabassi MA, Yao Y, Tour JM, Mayer TS, Allara DL (2005) *Nano Lett* 5:61–65.
24. Simmons JG (1963) *J Appl Phys* 34:1793–1803.
25. Simmons JG (1963) *J Appl Phys* 34:2581–2590.
26. Li X, He J, Hihath J, Bingqian X, Lindsay SM, Tao N (2006) *J Am Chem Soc* 128:2135–2141.
27. de Boer B, Frank MM, Chabal YJ, Jiang W, Garfunkel E, Bao Z (2004) *Langmuir* 20:1539–1542.
28. Engelkes VB, Beebe JM, Frisbie CD (2004) *J Am Chem Soc* 126:14287–14296.
29. Slowinski KS, Chamberlain RV, Miller CJ, Majda M (1997) *J Am Chem Soc* 119:11910–11919.
30. Schreiber F (2000) *Prog Surf Sci* 65:151–256.
31. Ulman A (1996) *Chem Rev* 96:1533–1554.
32. Yoshida T, Imafuku D, Alay JL, Miyazaki S, Hirose M (1995) *J Appl Phys* 34:903–906.
33. Brar B, Wilk GD, Seabaugh AC (1996) *Appl Phys Lett* 69:2728–2730.
34. Fujihira M, Inokuchi H (1972) *Chem Phys Lett* 17:554–556.
35. Esplandiu MJ, Noeske PLM (2002) *Appl Surf Sci* 199:166–182.
36. Brust M, Blass PM, Bard AJ (1997) *Langmuir* 13:5602–5607.
37. Rieley H, Kendall GK, Zemicael FW, Smith TL, Yang S (1998) *Langmuir* 14:5147–5153.
38. Deng W, Fujita D, Yang L, Nejo H, Bai C (2000) *Jpn J Appl Phys* 39:751–754.
39. de Boer B, Meng H, Perepichka DF, Zheng J, Frank MM, Chabal YJ, Bao Z (2003) *Langmuir* 19:4272–4284.
40. van der Marel C, Yildirim M, Stapert HR (2005) *J Vac Sci Technol A* 23:1456–1470.
41. Ulman A (1996) *Chem Rev* 96:1533–1554.